Foreshocks and delayed triggering of the 2016 M_W7.1 Te Araroa earthquake and dynamic reinvigoration of its aftershock sequence by the M_W7.8 Kaikōura earthquake, New Zealand

Emily Warren-Smith [a,*], Bill Fry [a], Yoshihiro Kaneko [a], Calum J. Chamberlain [b]

[a] *GNS Science, P.O. Box 30-368, Lower Hutt, 5040, New Zealand*
[b] *Institute of Geophysics, School of Geography, Environment and Earth Sciences, Victoria University of Wellington, Wellington, New Zealand*

ABSTRACT

We analyze the preparatory period of the September 2016 M_W7.1 Te Araroa foreshock–mainshock sequence in the Northern Hikurangi margin, New Zealand, and subsequent reinvigoration of Te Araroa aftershocks driven by a large distant earthquake (the November 2016 M_W7.8 Kaikōura earthquake). By adopting a matched-filter detection workflow using 582 well-defined template events, we generate an improved foreshock and aftershock catalog for the Te Araroa sequence (>8,000 earthquakes over 66 d). Templates characteristic of the M_W7.1 sequence (including the mainshock template) detect several highly correlating events (M_L2.5–3.5) starting 12 min after a M_W5.7 foreshock. These pre-cursory events occurred within ∼1 km of the mainshock and migrate bilaterally, suggesting precursory slip was triggered by the foreshock on the M_W7.1 fault patch prior to mainshock failure. We extend our matched-filter routine to examine the interactions between high dynamic stresses resulting from passing surface waves of the November 2016 M_W7.8 Kaikōura earthquake, and the evolution of the Te Araroa aftershock sequence. We observe a sudden spike in moment release of the aftershock sequence immediately following peak dynamic Coulomb stresses of 50–150 kPa on the M_W7.1 fault plane. The triggered increase in moment release culminated in a M_W5.1 event, immediately followed by a ∼3 h temporal stress shadow. Our observations document the preparatory period of a major subduction margin earthquake following a significant foreshock, and quantify dynamic reinvigoration of a distant on-going major aftershock sequence amid a period of temporal clustering of seismic activity in New Zealand.

© 2017 Elsevier B.V. All rights reserved.

1. Introduction

Large earthquakes are followed by aftershocks, the occurrence rates of which decay with time (Utsu et al., 1995). The highest numbers of aftershocks therefore occur immediately after the mainshock, and event detection using amplitude based methods can be problematic due to overlapping phases of large magnitude events (Peng et al., 2006). Furthermore, in instances where a significant foreshock precedes a larger earthquake, dense aftershocks from the first event may hinder detailed analysis of mainshock pre-cursors. In such cases, aftershock (and foreshock) catalog completeness is vital for both theoretical understanding (e.g. of triggering processes and post-seismic deformation) (Kilb et al., 2000) and science response (e.g. providing accurate seismic hazard forecasts following an event) (Ogata and Katsura, 2006).

Application of the matched-filter (or waveform correlation) method to aftershock sequences (e.g. Peng and Zhao, 2009) has resulted in the retrospective detection of many more earthquakes. This method detects events using *a priori* earthquake waveforms as templates, which are cross-correlated with continuous data to search for similar waveforms (Gibbons and Ringdal, 2006). Although such catalogs are still typically missing some early events in sequences, they can produce over an order of magnitude more detections than amplitude based methods alone (Frank et al., 2017; Warren-Smith et al., 2017).

Here we consider the September 2016 Te Araroa earthquakes in northeast New Zealand (Fig. 1), a complex offshore sequence including a M_W7.1 mainshock preceded 18.5 h earlier by a M_W5.7 foreshock. We analyze the temporal and spatial evolution of the sequence using a matched-filter detection routine to identify many events missing from the national catalog (Section 2.1). By computing precise cross-correlation derived phase arrivals, we calculate relative locations between key sequence events. Comparison of individual template responses, especially templates characteristic
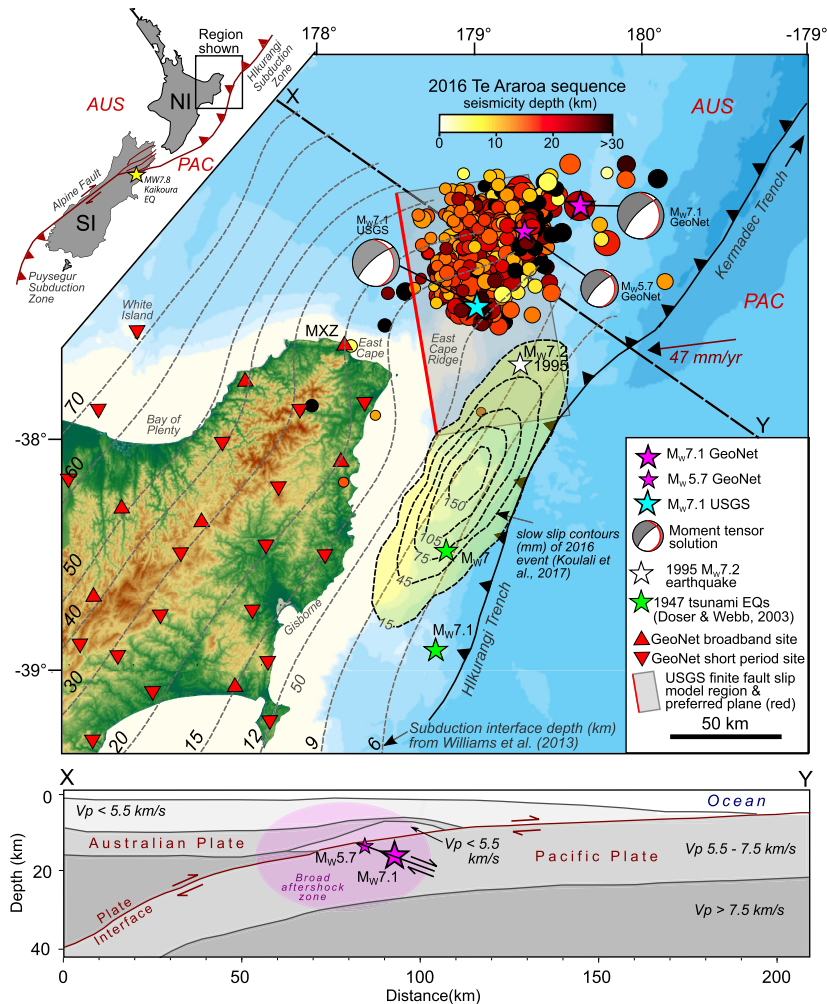
Fig. 1. Top: Overview of 582 GeoNet derived template locations from the Te Araroa sequence. Circles show seismicity colored by depth. Locations of the M_W7.1 and M_W5.7 foreshock from GeoNet are shown with pink stars, the global CMT mainshock location is shown with a cyan star. Moment tensor solutions are shown with the preferred plane in red. The grey shaded box represents the USGS finite fault model for the mainshock rupture patch. Dashed grey lines show the subduction interface contours from Williams et al. (2013). Dashed black lines and yellow shading shows the slip contours from the 2016 slow slip event (Koulali et al., 2017). Upright and inverted red triangles show the GeoNet broadband and short-period stations used respectively in this study. Corner inset shows tectonic setting of East Cape along the Australia (AUS) – Pacific (PAC) plate boundary zone. NI is North Island, SI is South Island. Bottom: Structural cross-section along line X–Y (top panel), showing tectonic setting of Te Araroa sequence. Plate model is based on the 2D velocity model along line RAU07-03 from Bassett et al. (2010). A low velocity (3.5 km/s < Vp < 5.5 km/s) zone of underplated sedimentary and crustal material immediately overlies the location of the Te Araroa sequence, which occurred within the subducting Pacific slab.

of the later mainshock sequence, allows us to test potential triggering mechanisms that led to the M_W7.1 Te Araroa earthquake (Section 3.4).

The Te Araroa sequence was followed by the M_W7.8 Kaikōura earthquake on 14th November 2016, ∼800 km to the southwest in north-eastern South Island (Hamling et al., 2017; Kaiser et al., 2017) (Fig. 1). These two 2016 M7+ earthquakes represent the latest major events occurring amid a decade of significant earthquake impacts in New Zealand, following the 2009 Dusky Sound, 2010–2011 Canterbury, and 2013 Marlborough earthquakes. We extend our matched-filter study to quantify the interaction between high dynamic stressing from passing Kaikōura surface waves and the progression of the aftershock sequence of the Te Araroa earthquake.

1.1. Northern Hikurangi seismicity and Slow Slip Events (SSEs)

The Hikurangi subduction zone lies at the southern end of the Tonga-Kermadec subduction system and accommodates near-orthogonal underthrusting of the Pacific plate beneath the Australian plate at a rate of ∼60 mm/yr in the Te Araroa region

(Beavan et al., 2002) (Fig. 1). The northern Hikurangi margin exhibits a diverse range of interrelated seismogenic phenomena, including shallow slow-slip events (SSEs) (Wallace and Beavan, 2010), large M > 7 tsunami earthquakes (Doser and Webb, 2003; Bell et al., 2014), microseismicity (Delahaye et al., 2009) and tectonic tremor (e.g. Todd and Schwartz, 2016). Previously documented major events include two M_W6.9–7.1 tsunami earthquakes in 1947 on the subduction interface, near shallowly subducted seamounts (Doser and Webb, 2003), resulting in slow velocity ruptures, and subsequent large tsunami (Bell et al., 2014). More recently, a shallow (12 km) M_W7.2 event occurred in 1995, to the south of the Te Araroa sequence, and a deeper (33 km) M_W7.1 event occurred close to the trench in 2001, followed by a M_W6.6 event three months later, close to the September 2016 epicenter (www.geonet.co.nz).

Northern Hikurangi SSEs occur repeatedly every 18–24 months, typically last for a few weeks and exhibit large (>10 cm) displacements. The Te Araroa sequence was preceded in August 2016 by a SSE with >15 cm of slip centered ∼70 km offshore, and extending farther north than previously observed events, as far as East Cape (Koulali et al., 2017) (Fig. 1). Mapping the northernmost ex-

tent of this SSE is limited by the lack of geodetic coverage nearby, but static Coulomb stress models (Koulali et al., 2017) show the SSE may have imparted up to 0.01 MPa of Coulomb stress increase on the southern end of the Te Araroa mainshock patch, and therefore possibly played a role in triggering the sequence.

1.2. The September 2016 Te Araroa sequence

The Te Araroa sequence began with a M_W5.7 foreshock at 22:04 on 31st August UTC followed by a M_W7.1 mainshock 18.5 h later. The largest aftershock was a M_W6.2 event ∼30 min after the mainshock. The mainshock was felt widely across North Island, and generated a 30 cm tsunami at Raukumara peninsula and Great Barrier Island (http://ptwc.weather.gov/).

The global CMT solution (Fig. 1) suggests a normal faulting mechanism, and a mainshock finite fault model (https://earthquake.usgs.gov/earthquakes/eventpage/us10006jbi#finite-fault) indicates complex slip on a shallow, east-dipping fault plane, initiating at 19 km depth. This depth is beneath the subduction interface (Williams et al., 2013), placing the source within the upper subducting Pacific slab (Fig. 1), however knowledge of the interface geometry is limited in this offshore region. Regional moment tensor solutions (Ristau, 2008) are consistent with this global model; both the M_W5.7 foreshock and M_W7.1 event show similar normal faulting mechanisms, with a shallow fault plane striking at ∼350° and dipping east at ∼20°, consistent with the finite fault model (Fig. 1). Manual aftershock locations from GeoNet appear elongate along subduction zone strike (Fig. 1), but this is likely an artifact of the network geometry and location algorithms (Section 1.4).

1.3. M_W7.8 Kaikōura earthquake and dynamic triggering

The Te Araroa mainshock was followed 74 d later by the M_W7.8 Kaikōura earthquake, which ruptured multiple strike-slip and reverse faults in northern South Island on the 13th November 2016 UTC (Hamling et al., 2017; Kaiser et al., 2017, Fig. 1). Dynamic shaking from the Kaikōura earthquake triggered multiple slow-slip events along the Hikurangi interface. Northern Hikurangi continuous GPS sites underwent 5–10 mm of eastward displacement within five hours of Kaikōura (Wallace et al., 2017), initiated by a strong northeast directivity effect and high dynamic stresses (100–600 kPa) from surface waves passing through low velocity forearc sediments.

Despite these conspicuous effects on interface slip, the effect of dynamic stresses on the evolution of the Te Araroa sequence has not been clear from the existing GeoNet aftershock catalog alone, although it suggests a dynamic response is possible. Globally, there are many examples of remote triggering of local earthquakes during and following the wave train of a large event (e.g. Hill, 2008; Gomberg et al., 2001; Prejean et al., 2004; Peng et al., 2010). Proposed triggering mechanisms include multiple processes such as changes in dynamic stress resulting in Coulomb failure (Hill, 2008), subcritical crack growth (Atkinson, 1984), and crustal fluid transport relating to permeability changes (i.e. the unclogging fracture model, Brodsky et al., 2003). Observed increased seismicity rates can last for several hours or days after the wave train, and follow a temporal Omori-type decay consistent with anticipated aftershocks of the initial wave train triggered events (Brodsky, 2006).

1.4. Motivations and aims

The Te Araroa sequence represents an intriguing case study for understanding triggering processes, in particular examining how a foreshock may trigger a larger mainshock nearby, as well as constraining interaction between two major earthquake sequences. Understanding such interaction, and mapping the spatiotemporal

evolution within the Te Araroa sequence has been inhibited predominantly by the ∼100 km epicentral distance from the nearest onshore station (Fig. 1). Additionally, the large azimuthal gap restricts accurate hypocenter determination, especially depths, given unclear S-phases. Furthermore, the effectiveness of routine detection algorithms based on short and long-term amplitude variations is restricted owing to emergent waveforms.

To overcome these limitations, we produce an improved foreshock and aftershock catalog for the Te Araroa sequence using a matched-filter method. In our analysis of this improved catalog we focus on two main objectives: (1) to quantify the relation between the M_W5.7 foreshock and the M_W7.1 mainshock (Section 3.4), in particular using template responses to trace pre-cursory activity, and (2) to identify any change in moment release within the Te Araroa source region, following dynamic stressing by passing M_W7.8 Kaikōura seismic waves (Section 3.5).

2. Methods

2.1. Matched-filter detection

We adopt the method of Gibbons and Ringdal (2006) for event detection, implemented using the open source Python package, *EQcorrscan* (Chamberlain and Hopp, 2016) and the workflow of Warren-Smith et al. (2017). For templates, we use 582 GeoNet detected aftershocks and foreshocks with manual phase picks (on 10–40 data channels, across 27 broad-band and short-period sensors). Both templates and continuous data (we use data between 6th August and 19th September 2016) are filtered between 1–10 Hz and down-sampled to 50 Hz. Template events are clipped to 1.5 s on each channel, starting 0.15 s before the phase-pick to exclude preceding random noise and scattered phases, yet allowing for possible pick error on emergent waveforms.

We calculate single channel normalized cross-correlation coefficients, ψ_s, which are then summed to give a network cross-correlation sum (CCS). A detection is made when CCS exceeds eight times the median absolute deviation. We calculate lag-times for each event (maximum allowed phase-arrival change of 2.5 s) and finally perform a round of quality control to remove all picks with $\psi_s < 0.2$, and all events with an average $\psi_s < 0.4$, and/or phase picks on fewer than 3 stations, which discards many false and low-quality detections.

All remaining events are then located within a 1D velocity model for the Raukumara peninsula (Reyners et al., 1999). If multiple events originate within six seconds (approximate timing errors of the most uncertain catalog locations), these duplicates are combined and assigned to the template of the detection that exhibits the highest mean ψ_s value.

2.2. Magnitude calculation

Waveforms are filtered between 1–20 Hz to exclude surface waves, station response is deconvolved and the response of a Wood–Anderson velocity seismograph is applied. The maximum peak-trough amplitude is then automatically picked from a variable window length (50% of the S-P time of the event at a particular station, beginning at the S-phase pick), before being corrected for the pre-filter and halved to estimate the true maximum amplitude. Local magnitudes, M_{Lv}, for individual stations are then calculated according to the same equation used for GeoNet magnitudes for ease of comparison between catalogs:

$$M_{Lv} = \log_{10} A - \log_{10} A_0 \tag{1}$$

where A is the velocity amplitude measurement in $\mu m\, s^{-1}$ and $\log_{10} A_0$ is a linearly interpolated distance dependent correction
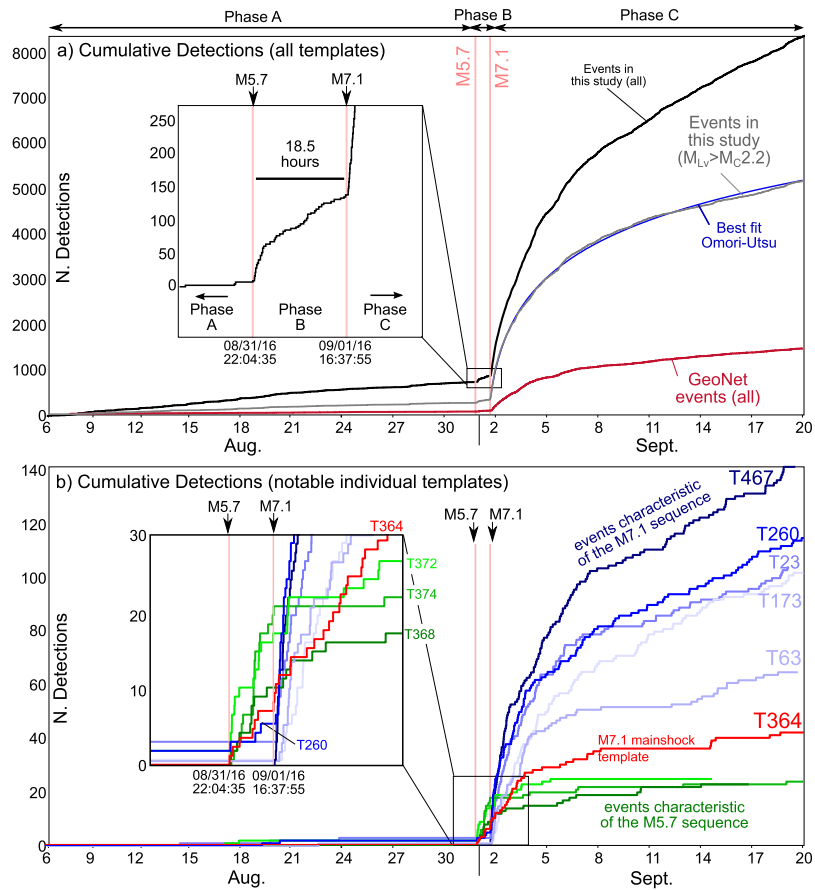
Fig. 2. Cumulative detections with time during the 66 d study period. a) All events detected by this study (black) and those cataloged by GeoNet (red). Detections shown a steady background rate in Phase A (prior to the M_W5.7 foreshock), followed by increases in rate during phases B (18.5 between the M_W5.7 and M_W7.1 events) and C (after the M_W7.1 event). Inset shows zoom on detections made in phase B. Grey line shows cumulative detection above the completeness magnitude (M_C2.2), with best-fitting Omori-Utsu decay model in blue. b) Cumulative detections made by key templates in the Te Araroa sequence. Blue lines are templates that dominate detections in phase C and are most characteristic of the M_W7.1 sequence. Green lines are the templates that dominate detections in phase B and are most characteristic of the M_W5.7 sequence. Red line shows the response of the M_W7.1 mainshock template (T364), which makes six detections in phase B prior to mainshock failure (see inset panel).
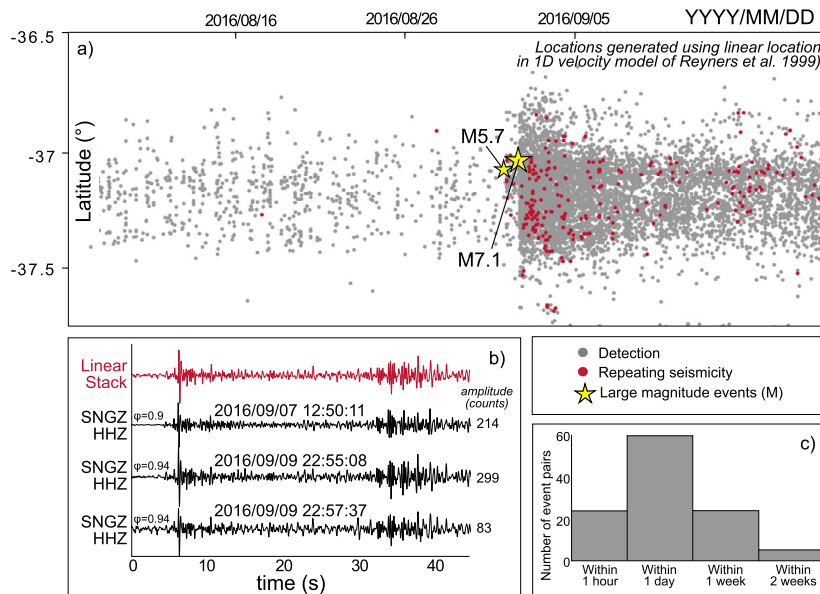

Fig. 3. Repeating seismicity detected throughout the Te Araroa sequence, defined by criteria in the main text. In total 141 repeater pairs are identified in 113 distinct families. a) Locations with time of all detections (grey), with repeating events (red) and major earthquakes (yellow stars) overlain. b) Waveforms of three repeating events (black) compared with linear stack (red) from the vertical channel of short period station SNGZ. c) Histogram of inter-event times for repeating event pairs. Most event pairs occur within one day of each other as doublets and triplets, before no further detections are made. (For interpretation of the colors in this figure, the reader is referred to the web version of this article.)

term, such that $\log_{10} A_0 = -3$ at 100 km epicentral distance. A final local magnitude is then calculated from the median station magnitude across all recording stations.

3. Results

Using the methods outlined in the previous section, we identify 8,366 distinct events in the Te Araroa region over 66 d (Fig. 2a). This represents an approximately five-fold increase relative to the GeoNet catalog for the same time period ($\sim$1,900).

To simplify terminology in reference to foreshocks and aftershocks (as aftershocks of the $M_W 5.7$ event are still foreshocks to the $M_W 7.1$ event), we hereafter refer to the sequence as exhibiting three phases (Fig. 2a). Phase A includes all events in the catalog occurring before the $M_W 5.7$ event. Phase B includes events in the 18.5 h between the $M_W 5.7$ and $M_W 7.1$ events, and phase C includes all events in our catalog occurring after, and including, the $M_W 7.1$ mainshock. These phases of seismicity are discussed further in Sections 3.3–3.4.

The absence of clear S-phases, and the limited azimuthal coverage of the network promote uncertainties in depth estimates, more so than in epicenter. As such, we focus our discussion (Sections 3.4, 4) on the temporal evolution of the sequence, and relative locations of key events only.

3.1. Repeating seismicity

We identify repeating events (representing repeated failure of the same point in space), using the criteria of $\psi_s > 0.95$ on >4 stations and unfiltered data. We correlate every detected event with every other detection in the catalog and group repeaters into families of waveforms meeting these criteria.

In total 141 repeater pairs, in 113 distinct families (maximum of five repetitions per family) are detected. Repeaters are almost exclusively confined to phases B and C and occur within one day of each other as doublets or triplets (Fig. 3). We detect no significant repeating events during phase A, possibly indicating an aseismic process on the normal fault plane was not active before the sequence, or that not enough slip occurred for patches to be re-stressed to failure. However, it may also be possible that our templates, which were sourced predominantly from the aftershock sequence, are not suitable to distinguish whether any driving aseismic slip on other structures, such as the plate interface, occurred in the near vicinity.

3.2. Magnitudes

We obtain local magnitudes, M_{Lv}, for 97% of events ($n = 8,077$). The major foreshock magnitude is unchanged ($M_{Lv} 5.7$), but our mainshock magnitude is lower at $M_{Lv} 6.8$ (versus $M_W 7.1$). This may be due to local magnitude scale saturation at high magnitudes, inclusion of fewer regional stations, or hypocentral location differences. Our mainshock hypocenter locates $\sim$10 km farther offshore than the GeoNet location, which we calculate contributes $\sim$0.1 magnitude units of overestimation; the difference is therefore most likely attributable to magnitude scaling or network effects.

The magnitude frequency distribution for detected aftershocks (Fig. 4) exhibits a Gutenberg–Richter relationship with a b-value of 0.76 and completeness of $M_{Lv} 2.2$, calculated using a maximum likelihood approach. The GeoNet catalog exhibits a bimodal distribution, which we do not observe. Instead we attribute this bimodality to differences between automatically located and reviewed events; in the GeoNet catalog automatically located events typically locate closer to shore than manually located ones, and their magnitudes are hence underestimated. Our detection routine has predominantly increased the number of detections with
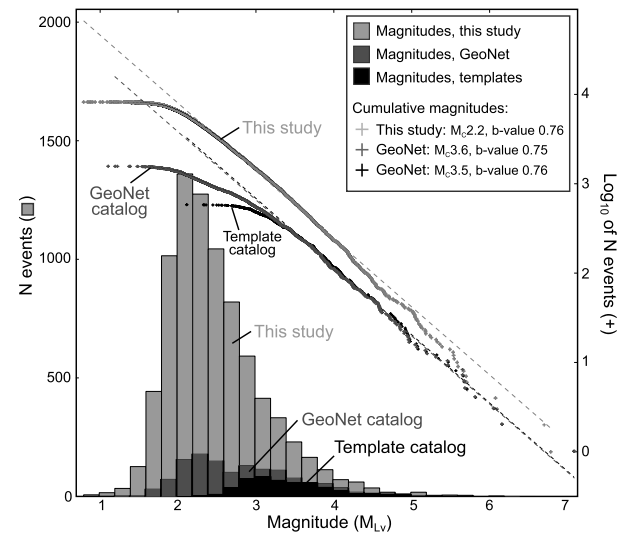

Fig. 4. Magnitude frequency relationships for three Te Araroa sequence catalogs (6th August–19th September 2016) discussed in this study. Black shows manually picked events utilized as templates, which were sourced from the full GeoNet catalog (mid-grey, includes unreviewed events). The lightest grey shows events detected in this study using a matched-filter approach. Bars show the total number of events for magnitude bins size 0.2, crosses show the cumulative frequency in the log domain, the slope of which defines the b-value of the Gutenberg–Richter relationship. Dashed line shows linear fit. The b-value for all three catalogs is very similar (0.75–0.76), but our matched-filter method has improved the magnitude of catalog completeness (M_C) by 1.4 units to $M_C 2.2$.

$M_{Lv} < 4$, but has also identified more $M_{Lv} > 4$ events occurring very early in the sequence, that were likely missed because of overlapping larger events, or were automatically mislocated and hence their magnitudes were initially underestimated.

3.3. Detections in phase A: events prior to the $M_W 5.7$ foreshock

In the 25 d prior to the $M_W 5.7$ foreshock, we detect 734 events, defining an average background rate of $\sim$30 events/day (Fig. 2a). The average ψ_s for these detections is 0.56, indicating they are sufficiently similar to aftershock templates to exceed the detection threshold, yet are unlikely to represent complete failure of the same asperities. These events exhibit no spatial clustering; we therefore interpret them to be representative of the diffuse background seismicity rate. We observe no acceleration in detection rate or moment release in the days immediately prior to the $M_W 5.7$ foreshock. Nor do we observe any increase in seismicity rate corresponding to the initiation of the preceding SSE in late August (Koulali et al., 2017).

3.4. Detections in phases B and C: events in the aftershock sequences of the $M_W 5.7$ and $M_W 7.1$ events

Phase B and C events dominate detections, with 131 earthquakes over 18.5 h in phase B, and 7,519 earthquakes over 19 d in phase C. Our final $M_W 7.1$ aftershock catalog exhibits an Omori-type decay (Fig. 2a). After correcting for catalog completeness, we calculate the modified-Omori decay parameters ($n(t) = K/(t+c)^p$) after Utsu et al. (1995) using a bootstrap approach to be $p = 0.98$, $c = 0.454$ and $K = 1267.9$ for events in phase C. Too few aftershocks of the $M_W 5.7$ remain after completeness correction to reliably calculate these parameters for phase B.

Templates most characteristic of both the $M_W 5.7$ and $M_W 7.1$ aftershock sequences (those templates which dominate the detections in each case) (Fig. 2b) can be utilized as 'source-tracers' to identify activity relating to the respective sequences. Templates
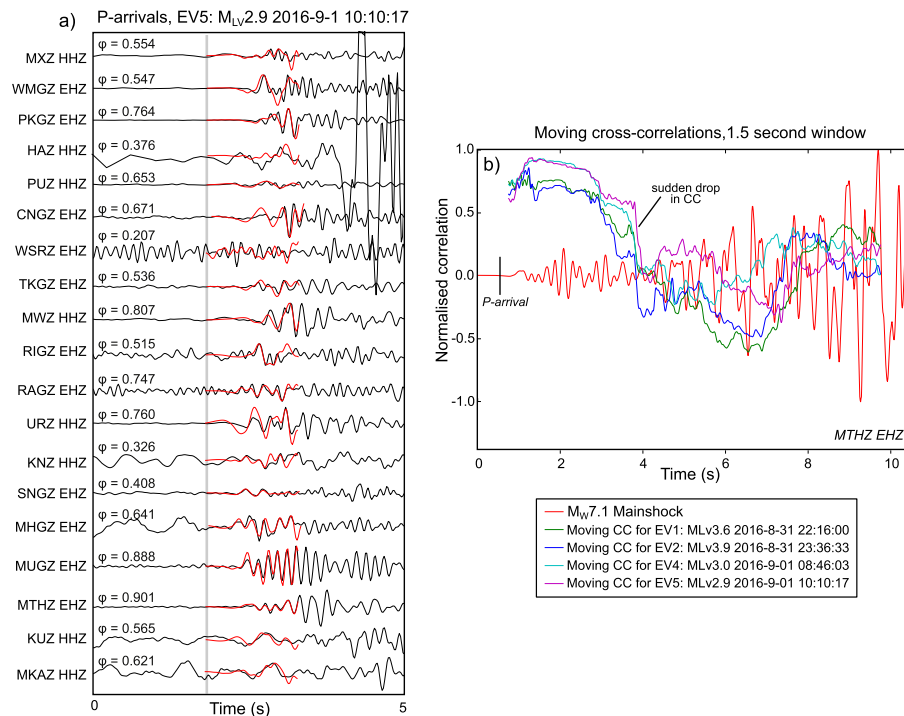
Fig. 5. a) Waveform comparison between the M_W7.1 mainshock (red template waveforms) and a M_{Lv}2.9 event in phase B (Event EV5, origin time 2016-09-01 10:10:17, black waveforms) detected by the mainshock template. All waveforms are vertical channels filtered 1–10 Hz, and are aligned on the direct P-arrival phase. Normalized single-channel cross-correlation coefficients (phi) between the template and detected event are plotted next to each trace. b) Moving cross-correlations for unfiltered waveforms between four phase B precursory events (green, blue, cyan and purple lines), and the P-phase of the M_W7.1 mainshock (red) on the vertical channel of station MTHZ. Cross-correlations are computed within a 1.5 s window, and all show strong waveform similarity between the mainshock and the smaller events for the first 3.5 s after the P-arrival.

T368, T372 and T374 (green lines in Fig. 2b) are most characteristic of the M_W5.7 aftershock sequence, and together detect ∼36% of events in phase B. These templates exhibit a sharp increase in detection rate immediately following the M_W5.7, and show no secondary response to the M_W7.1, suggesting no or limited additional activation of the M_W5.7 rupture patch by the mainshock. Templates T23, T63, T173, T260 and T467 are most characteristic of the M_W7.1 aftershock sequence, each detecting >60 events, and together detect 7% of events in phase C (blue lines in Fig. 2b). The other events in this phase are comprised of a small number of detections-per-template across other templates, indicating a wide and otherwise diverse aftershock zone.

Interestingly, several templates characteristic of the M_W7.1 sequence make detections in phase B, most notably the mainshock template, T364, which makes five detections during this time (red line in Fig. 2b). These detected events range in magnitude between M_{Lv}2.9 and M_{Lv}3.9, the first occurring 12 min after the M_W5.7. Some of these events were detected by other templates, but were assigned to template T364 during declustering, as this template correlated the best out of the 582 templates despite, notably, being the largest magnitude template used, and the sequence mainshock. Arrival times across the network of these phase B events are negligibly different from the mainshock, and some channels correlate very well (e.g. MTHZ HHZ $\psi_s = 0.905$ for a M_{Lv}2.9 event, Fig. 5). Even for unfiltered waveforms (Fig. 5b), we show that strong ($\psi_s > 0.75$) normalized cross-correlations between the P-phase of the mainshock and the pre-cursory events exist for at least 3.5 s after the direct P-arrival.

We investigate the spatial relation between these precursory events and the mainshock by calculating double-difference relative hypocenters (Waldhauser, 2001). We implement catalog and cross-correlation pick times, and initial locations computed using the 1D velocity model with our correlation-corrected picks. This relocation (Fig. 6) shows that all five precursory events locate very

close to the mainshock hypocenter, within 1.2 km horizontally and 1 km vertically, placing them within the rupture patch size of the mainshock. These events locate ∼40–50 km to the northeast of the events characteristic of the M_W5.7 sequence (green circles in Fig. 6).

These observations indicate a clustering of activity distinct from other foreshock phase B events, very similar to, and close in time and space to the mainshock, possibly triggered by the M_W5.7 foreshock. Further discussion on the implications for these high correlations, and the physical context of these pre-cursory events is included in Sections 4.1 and 4.2.

3.5. Static Coulomb stress models

We examine potential triggering mechanisms for this phase B activity by calculating the static Coulomb stresses from the M_W5.7 foreshock and the M_W7.1 mainshock (Fig. 7) using the Coulomb 3.3 software (Toda et al., 2011). Because of uncertainties in the nodal versus auxiliary plane, we perform a series of calculations for each possible combination of shallowly dipping (strike/dip/rake = 354°/21°/−138°) and steeply dipping (strike/dip/rake = 224°/76°/−74°) planes of the moment tensor, for both the source and receiver faults (Figs. 7a–j). We utilize the empirical relations of Wells and Coppersmith (1994) to estimate rectangular source dimensions of the two normal events based on their moment magnitudes. For the shallowly dipping mainshock source, we additionally implement the USGS finite fault slip distribution. We use an effective coefficient of friction of 0.4, and compute the resulting stress changes at 19 km depth (the hypocentral depths of the events). We observe similar results for a range of friction coefficients between 0.3 and 0.7. We constrain the inter-event distance and azimuth from our relative relocation approach, as outlined previously.
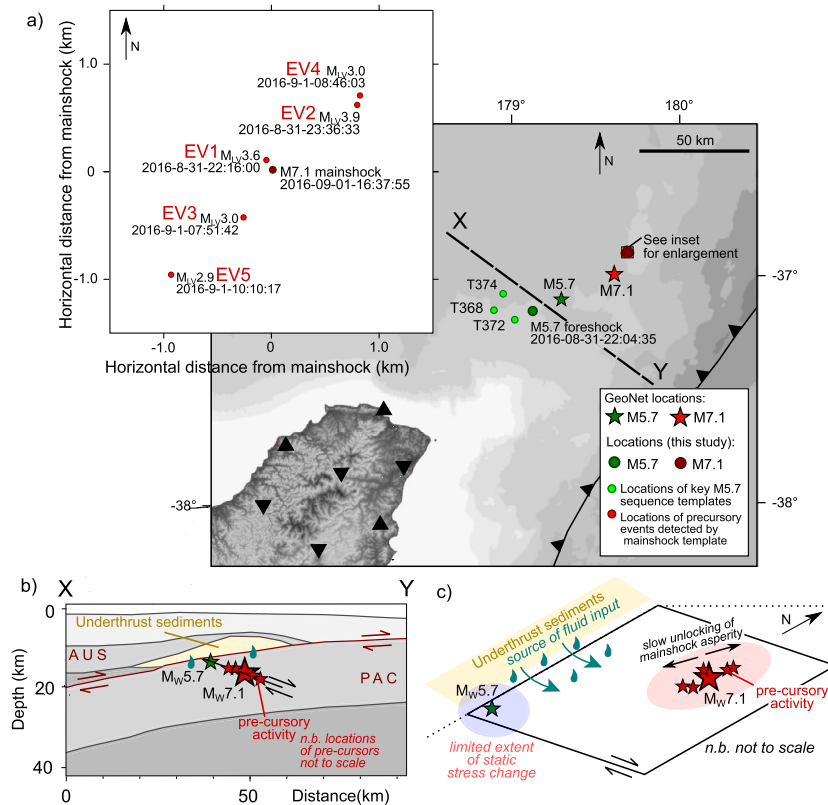
Fig. 6. a) Locations of key events in the Te Araroa sequence as constrained by this study (circles) and by GeoNet (mainshock and foreshock only, shown as stars). Main map shows large-scale locations of the sequence. Light green circles show the locations of templates most characteristic of the M_W5.7 aftershock sequence, which detect ~36% of events in phase B, and locate close to the M_W5.7 foreshock hypocenter (dark green circle). Red circles show M_W7.1 characteristic events which locate ~40–50 km to the north-east from M_W5.7 events. Inset shows double-difference relative relocations of events detected by T364 (mainshock) during phase B. These events all occur within 1.2 km of the mainshock location, initiating a few minutes after the M_W5.7. b) Structural cross-section showing schematic locations of the foreshock, mainshock and pre-cursory events in relation to underthrust sedimentary material as constrained by Bassett et al. (2010). c) Schematic model of the fault plane, showing locations of key events, and proposed aseismic unlocking of the mainshock rupture patch prior to failure.

Our models show that the M_W5.7 foreshock imposed low ($\ll$1 kPa) static Coulomb stresses at the M_W7.1 hypocenter, and where the precursory events occurred, regardless of orientation. This indicates static coseismic foreshock stressing is unlikely to be the cause of the triggered pre-cursory activity and the eventual mainshock. Conversely, higher (~50 kPa) positive stresses are imposed by the M_W7.1 mainshock at the foreshock location, but only for a steeply dipping mainshock source fault (Figs. 7e, h). The inclusion of the finite fault slip inversion in the calculations (Fig. 7g, j) highlights the oversimplification of the uniform slip models, and exhibits complex patches of positive and negative stress changes within the much larger modeled fault region, but with no significant stress changes extending to the M_W5.7 hypocenter. This appears consistent with the lack of observed secondary response in M_W5.7 characteristic templates following the mainshock (green lines in Fig. 2b), as these template locations experienced no significant positive static Coulomb failure stress change.

3.6. Events following M_W7.8 Kaikōura earthquake

3.6.1. Calculation of dynamic Coulomb stresses

Implementing the method of Wallace et al. (2017) and Holden et al. (2017) we calculate dynamic Coulomb stresses, in the period range $\geq$3 s, occurring in the Te Araroa region from the passing of Kaikōura surface waves (e.g. Kilb et al., 2000). We resolve the resulting calculated stress perturbations onto the preferred fault plane from the USGS finite fault model, and calculate the maximum dynamic Coulomb stress according to King et al. (1994), for

two end member values of the effective friction coefficient, $f = 0.1$ and $f = 1.0$.

Our results indicate the resolved dynamic stresses on the Te Araroa source plane from the Kaikōura earthquake are considerable (~70 kPa for $f = 0.1$ and ~150 kPa for $f = 1.0$), and ~100 times larger than the static Coulomb stress change (<1 kPa). Peak dynamic stresses occur ~300 and 400 s after the Kaikōura origin time (Fig. 8b).

3.6.2. Search for triggered seismicity

We perform an additional search for seismicity in the Te Araroa source region occurring over a three-day period spanning the M_W7.8 Kaikōura Earthquake (12th–14th November 2016, UTC). We include three new templates in our search, which range in magnitude from M_W2.8 to a M_W5.1 occurring four hours after the Kaikōura earthquake (www.geonet.co.nz). We apply the same workflow as in Section 2.1, but increase the bandpass filter to 5–20 Hz, to isolate higher frequencies dominant in local seismicity from regional Kaikōura phases. We calculate approximate local magnitudes for these detections, but note that our magnitudes are overestimated in many cases, as we do include longer-periods (<5 Hz) in our pre-filter when picking amplitudes (which are contaminated by the passing wavetrain of the Kaikōura aftershock sequence). We then convert local M_{Lv} magnitudes to moment magnitudes, M_W, and then to seismic moment, M_O, using the relationship derived by Ristau (2009) to illustrate the relative, rather than the absolute pattern of moment release (Fig. 8).
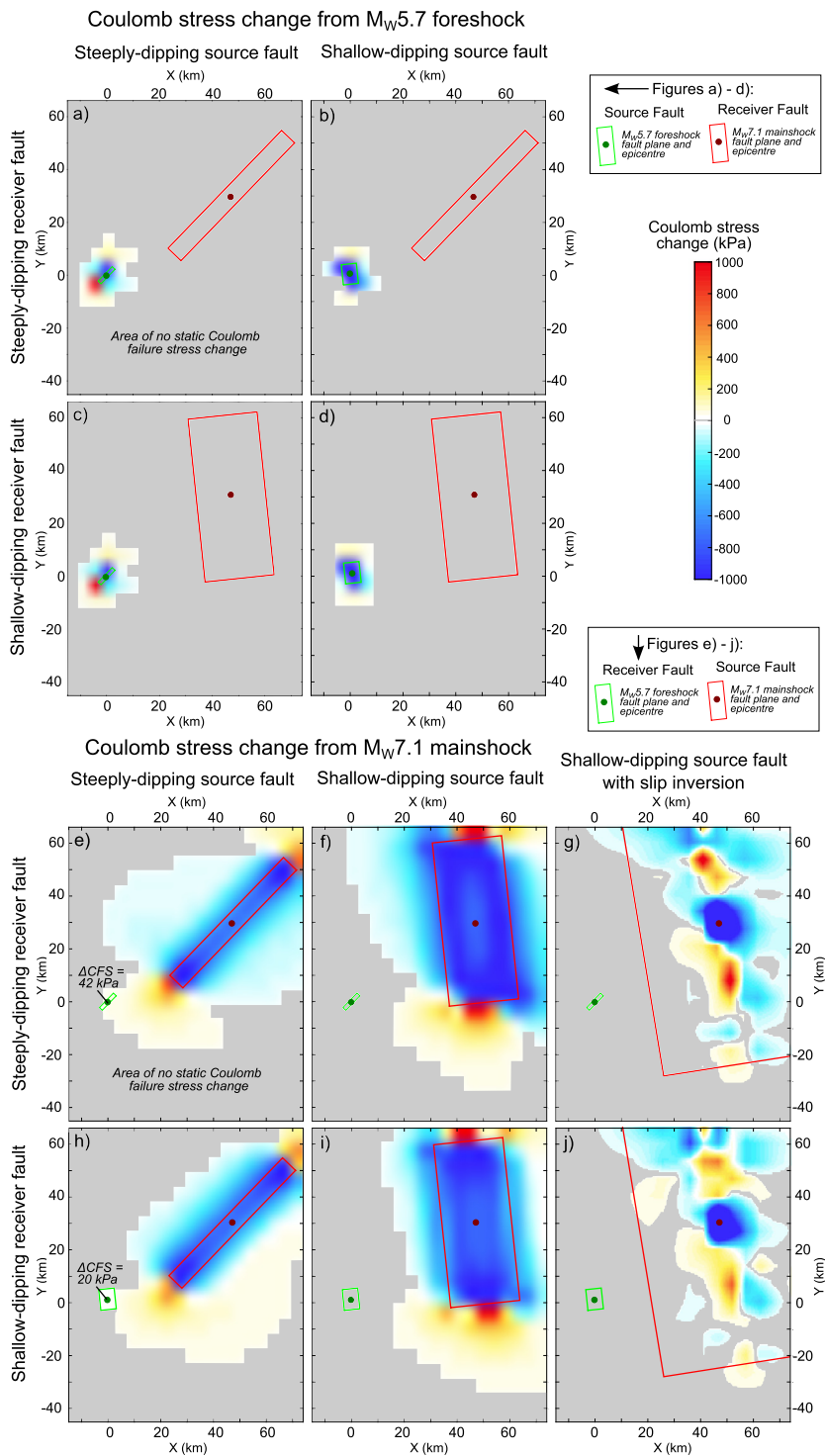
Coulomb stress change from M$_W$5.7 foreshock

Coulomb stress change from M$_W$7.1 mainshock

Fig. 7. Calculated static Coulomb stress changes (in kPa) resulting from the M$_W$5.7 foreshock (a–d) and the M$_W$7.1 mainshock (e–j). In each subplot, the green and red circles show the foreshock and mainshock hypocenters respectively, and their fault dimensions are shown by the green and red rectangles respectively. All possible combinations of shallow-dipping (strike/dip/rake = 354°/21°/−138°) and steeply-dipping (strike/dip/rake = 224°/76°/−74°) source and receiver faults are used based on the two possible moment tensor planes. Subplots g) and j) implement the USGS finite fault solution as input for the mainshock slip distribution on the shallow-dipping fault plane. All other models implement a uniform slip distribution based on a source defined by empirical dimensions from Wells and Coppersmith (1994). Figures show a depth slice at 19 km, and are calculated using an effective coefficient of friction of 0.4. Grey shaded areas denote where no change in Coulomb failure stress was modeled.

The following observations are noted regarding detections in the Te Araroa source region (Fig. 8). These observations are discussed further in Section 4.3.

1. We make 39 detections, all M$_{LV}$ < 3.5, in the 35 h prior to the occurrence of the Kaikōura earthquake (Fig. 8).

2. A sharp increase in detection rate begins ∼210 s after the Kaikōura origin time, with the arrival of the S-waves in the Te Araroa source region, and continues through the highest modeled dynamic stresses from passing surface waves (Fig. 8b). We observe higher rates of detections occurring at ∼300 and ∼400 s after Kaikōura (Fig. 8b). This period of heightened
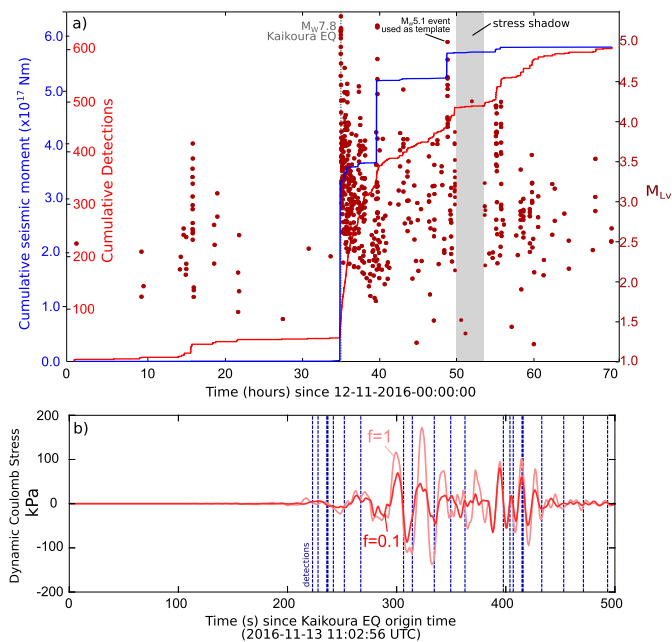
Fig. 8. Response of the Te Araroa aftershock region to passing wave train of the M_W7.8 Kaikōura earthquake. a) Cumulative detections with time (red line) for a three-day period centered on the Kaikōura earthquake. Detections show a sudden rate increase immediately following the arrival of the regional waves. Cumulative moment release (blue line) is shown as calculated from the detection M_{Lv} magnitudes (red circles). This calculated moment release is an overestimate, owing to local events being buried in regional high amplitude signals, but shows a similar pattern to the cumulative detections. b) Red lines show synthetic dynamic Coulomb stresses (for effective friction coefficients $f = 1.0$ and $f = 0.1$) imposed by the M_W7.8 Kaikōura earthquake, as resolved on the USGS derived Te Araroa fault plane with a focal depth of 19 km. Vertical blue dashed lines denote origin times of detections made using Te Araroa aftershock templates, and correspond to period of highest modeled dynamic stressing.

seismicity rate includes >300 detections over ∼4 h, and terminates with the M_{Lv}4.9 (M_W5.1) template event (the largest event in the GeoNet catalog over this time).

3. This is followed by a pause in detections, with only three detections occurring during a three-hour period (grey bar in Fig. 8a). We interpret this pause in detections to be a temporal stress shadow, incited by a dynamically triggered clock-advance of moment release in the previous five hours (Section 4.3).

4. Once detections resume after the pause, the detection rate decays and by ∼36 h after Kaikōura, is similar to the original, pre-Kaikōura rate.

The β-value describes the difference between the observed number of events after Kaikōura and the expected number from the background rate (Matthews and Reasenberg, 1988). After correcting for the catalog completeness, we calculate the β-value between the two time periods (the 37 h after Kaikōura, and the full three day period shown in Fig. 8a) to be positive at $\beta = 20.62$. Absolute β-values ≥ 2.57 are indicative of statistically significant rate increases at the 99% confidence level. Our β-value greatly exceeds this, and even though our magnitudes include large uncertainties and hence completeness influences may not be fully removed, we argue that a statistically significant seismicity rate increase occurs in the Te Araroa source region following the Kaikōura earthquake.

4. Discussion

The Te Araroa sequence is intriguing for a number of reasons, most notably because of the range of earthquake interaction processes it exhibits between local, regional and aseismic events.

Firstly, the sequence was preceded in August by a slow slip event on the northern Hikurangi interface (Fig. 1), which may have acted as an initial static stress trigger for the sequence (Koulali et al., 2017). Secondly, our matched-filter results build on modeling of Koulali et al. (2017) to indicate that precursory activity, very similar in location and waveforms to the mainshock, was subsequently dynamically triggered by the M_W5.7 foreshock. Finally, the ongoing aftershock sequence was reinvigorated two months later by dynamic stressing from the M_W7.8 Kaikōura earthquake, some 800 km away.

4.1. How did the M_W5.7 foreshock trigger the M_W7.1 mainshock?

Results outlined in Section 3.4 reveal that precursory activity located very close, and with waveforms similar to the M_W7.1 mainshock was initiated a few minutes after the M_W5.7 foreshock, some 40–50 km away, and continued for several hours before the largest event. Walter et al. (2015) observe a similar triggering of foreshocks prior to the September 2012 M_W7.6 Nicoya earthquake following the August 2012 M_W7.3 El Salvador earthquake, 450 km away. In that case, the distances involved suggest that dynamic, rather than static, loading is a likely triggering mechanism responsible for the Mw7.6, even though it occurred about a month later than the M_W7.3. At shorter distances, such as those of a few rupture lengths involved in the Te Araroa sequence, there is no widely accepted understanding of whether static stresses arising from fault slip (e.g. King et al., 1994) or dynamic stresses from passing seismic waves generated by seismic slip (e.g. Kilb et al., 2000; Gomberg et al., 2001) are more important.

Coulomb stress models (Section 3.5) indicate that coseismic static stresses imposed by the foreshock on the mainshock hypocenter were small, and therefore unlikely to have triggered the mainshock; the inter-event distance is too large. Instead, it is likely that dynamic processes resulting from the M_W5.7 triggered the M_W7.1. One interesting feature of the catalog is the time delay involved between foreshock and mainshock initiation. Numerical studies show that dynamic stresses can trigger a delayed response, with an Omori-law decay, as the result of changes to the critical slip distance, D_C, (e.g. Parsons, 2005) arising from strain induced compaction, pore fluid migration (Bosl and Nur, 2002), triggered aseismic creep (Shelly et al., 2011) or associated increased loading from afterslip (Perfettini and Avouac, 2004).

In light of the limited seismic and geodetic network coverage of the area, we cannot conclude definitively which of these mechanisms, or combination of mechanisms, contributed to the triggering of the M_W7.1. However, we propose that the mainshock was likely triggered by a preparatory aseismic creep process (e.g. Lohman and McGuire, 2007), or pore fluid migration (e.g. Bosl and Nur, 2002) activated by dynamic stresses from the M_W5.7. In what follows, we discuss the compatibility of our observations with these proposed scenarios.

Our rationale for a preparatory aseismic creep scenario during Phase B is outlined as follows. Firstly, the cumulative rate of mainshock template (T364) detections (red line in Fig. 2b) is initially approximately linear (during phase B and the first 2 d of Phase C), suggesting seismicity sampled by this template may be driven by an underlying process other than cascading earthquakes triggering additional events in a power-law dictated setting (Vidale and Shearer, 2006). Secondly, pre-cursory Phase B events begin closest in space to the mainshock hypocenter, and extend outwards bilaterally, suggesting slow unlocking of the M_W7.1 asperity (Fig. 6c) over the course of several hours. If this is the case, we may expect to observe repeating seismicity, such as that documented by Kato et al. (2012) and Kato and Nakagawa (2014) prior to both the 2011 Tohoku-Oki and 2014 Iquique earthquakes. Our analysis of repeating earthquakes (Section 3.1 and Fig. 3) indicates although

we observe repeating seismicity during Phase B, these events do not locate close to the $M_W7.1$ hypocenter. It is, however, possible that the short duration of Phase B may not be sufficient to observe such repetitions of single asperity failure within all areas sampled by the templates.

Such preparatory aseismic slip in Phase B may have simply triggered the failure of the mainshock asperity (e.g. Lohman and McGuire, 2007) or be similar to observations of nucleation processes in numerical and laboratory analogue experiments (e.g. McLasky and Kilgore, 2013; Kaneko et al., 2016). Small Phase B foreshocks then represent rupturing of smaller-scale asperities that were triggered by the aseismic slip, and the mainshock nucleation represents the failure of a larger asperity in the vicinity of these foreshocks (e.g. Kato and Nakagawa, 2014). For some unknown reasons relating to conditions near the epicenter, the mainshock failure started as a rupture process similar to that of these foreshocks in the first few seconds, but with a different amount of slip, as reflected in the similar shape, but different amplitudes of the initial few seconds of the waveforms.

Alternatively, dynamic foreshock stressing may have unclogged fluid pathways leading to permeability enhancement (e.g. Elkhoury et al., 2011) near the mainshock hypocenter, and subsequent pore fluid migration directly triggered small Phase B foreshocks and eventually the mainshock asperity. Fluids play a pivotal role in controlling the locations and rates of both aftershock and swarm sequences, either through a rise in fluid pressure (e.g. Ake et al., 2005) or dynamic redistribution of fluids. This process is considered especially important in subduction slab earthquakes, where tensional fracturing in the upper part of the subducting plate provides conduits for fluid migration (Ranero et al., 2003). The Te Araroa sequence occurred directly beneath a low velocity zone of underplated sedimentary material (Fig. 6b, Bassett et al., 2010), which we propose provides a nearby source of fluids within a highly porous medium (12–18% at depths of 5–20 km, Bassett et al., 2010). We note that the time period and distance between precursory events EV1 and EV4/5 (Fig. 6) is ∼12 h and ∼1 km, indicating fluid diffusivity of ∼2 m^2/s, which is similar to values reported by Shelly et al. (2016) and Goebel et al. (2017) based on seismicity migration patterns.

4.2. Magnitude relation and implications for earthquake scaling

Our matched-filter results show that the first few seconds of waveforms of the $M_W7.1$ earthquake are very similar in nature to events as small as $M_{Lv}2.7$, across more than four orders of magnitude (Fig. 5). Large magnitude earthquakes are inherently more complex than smaller magnitude events, rupturing larger areas and including more complicated source-time functions, often slipping across multiple separate faults (Geller, 1976). Despite this, matched-filter detection shows that waveform similarity of body phases is possible over several orders of magnitude, as large magnitude templates (M5.5+) are capable of detecting events up to hundreds to thousands of times smaller (e.g. Warren-Smith et al. (2017) detected a $M_L1.5$ event using a $M_L5.8$ template in a 1–10 Hz frequency band).

Detections made by a single template are, by design, restricted to be close both in spatial location, and source mechanism. Therefore, the above observations pertain to the magnitude scaling characteristics of individual fault patches. Ultimately, the maximum possible magnitude difference between template and detection is likely related to a number of factors, including the bandpass frequency chosen during processing, number and spatial density of templates utilized, spatial variability in the sequence, and length of the template waveform and allowed lag-time windows, and is therefore both sequence and workflow specific.

In the case of the Te Araroa sequence, the difference in single-phase network response is mitigated by the fact that the network azimuth is so small (i.e. the declustering process is most sensitive to differences in the shape of the waveform, rather than the timing of arrivals across the network). Furthermore, the epicentral difference between the $M_W5.7$ and the $M_W7.1$ when compared to the epicentral-station distances across the network is relatively small, implying large-scale shared path effects between the two sequences. Together with the high normalized single-channel cross-correlations, and in particular the same polarities, between the detections and the mainshock, we argue that such similarities between the mainshock and pre-cursory events represent not only spatial similarities, but also similar source properties.

If this is the case, then it indicates that the rupture process of the smaller events is initially highly correlated with the larger event, and additional complexity associated with later stages of mainshock rupture only occurs ∼3.5 s after nucleation. By considering a large magnitude event as one that cascades to exceed the asperity dimensions of a smaller event, this may suggest the size of the smaller magnitude asperity is characterized by this 3.5 s time period. Typical rupture durations, τ, for M < 4 earthquakes are of the order of $\tau < 1$ s (Aki and Richards, 2002). It is possible that $\tau = 3.5$ s for pre-cursory events instead represents much slower ruptures, including the possibility of a lower fault rigidity or a large source radius. We are only able to speculate on this; accurate calculation of the source parameters of these events is not possible given the large (>120 km) distances between source and the closest station.

4.3. Dynamic triggering by $M_W7.8$ Kaikōura earthquake

A statistically significant increase in seismicity rate occurred during and immediately following the arrival of the $M_W7.8$ Kaikōura earthquake wavetrain in the Te Araroa source region (Section 3.6.2). Given uncertainties in the synthetic wavefield, we cannot directly compare these timings of triggered events to peaks in the synthetic dynamic stress perturbations to identify a relationship between the two. However, at the dominant period of the synthetic stresses (10–20 s), the synthetic velocity waveforms correlate well with observed data at stations in East Cape, so the timing errors on the shorter period stress perturbations are likely to be small. We are confident that the estimated arrival times of the dominant phases are well constrained (i.e. that higher dynamic stresses occur at ∼300 and ∼400 s after the Kaikōura earthquake, Fig. 6b). These periods correspond to times of increased detection rate, indicating a direct link between peak dynamic stresses and seismicity.

We observe a three-hour lull in detection rate shortly following a triggered $M_W5.1$ event (grey bar in Fig. 8a). We interpret this as a temporal stress shadow; the natural occurrence rate of events in the region has been accelerated, and hence requires a period of time to recover where the fault patches that were slightly behind in reaching failure take time to catch up. This phenomenon has been previously observed globally following remote dynamic triggering, for example in Tibet following the 2004 Sumatra earthquake (Yao et al., 2015) and global rates of M5+ earthquakes following the 2012 Indian ocean earthquake (Pollitz et al., 2012). Our observations are the first to document this process occurring in an ongoing major aftershock sequence hundreds of kilometers away.

As such, our results have direct implications for seismic hazard models. At a time when New Zealand is still experiencing aftershocks from several major sequences, including the 2010 Canterbury and 2013 Cook Strait earthquakes, such reinvigoration by subsequent events may incidentally increase hazard at considerable distances from, and outside the immediate aftershock zone of contemporary events. Re-acceleration in the Te Araroa sequence was initially missed, not only because the triggered events were

difficult to detect using amplitude based methods, but also because the high productivity rates immediately following the Kaikōura earthquake meant the GeoNet detection algorithm favored higher magnitude events farther south. Our improved catalog shows that many events, including some high magnitude events, were missed, thus likely changing the on-going forecast for the Te Araroa sequence. However, quantifying the moment release during this triggered period is difficult owing to triggered events being buried within high amplitude regional waveforms. Further work is required to accurately quantify this moment release, and feed the improved catalog into the hazard forecasts.

5. Conclusions

Incomplete aftershock and foreshock catalogs of large events frequently preclude detailed analysis of sequence initiation, evolution and triggering processes. Matched-filter methods offer improved resolution of the spatial and temporal progression of sequences, often not obtainable using amplitude-based detection alone. By applying such methods to the northern Hikurangi margin, New Zealand, we analyze the 2016 M_W7.1 Te Araroa earthquake. We show that the M_W7.1 mainshock, when used as a template, detects several highly correlating events occurring 12 min after a major M_W5.7 foreshock (which occurred ~50 km away). These high-correlation events provide evidence for precursory activity, in a similar location, and with similar source properties to the largest event, prior to mainshock failure, initiated by a nearby foreshock. This preparatory phase was unlikely to be statically triggered and hence represents a delayed dynamic process likely controlled by the presence of fluids and/or an aseismic creep process. Furthermore, we extend our study to show that the Te Araroa aftershock sequence was dynamically reinvigorated two months later by the M_W7.8 Kaikōura earthquake, 800 km to the southwest, following high dynamic Coulomb stresses of up to 150 kPa.

Acknowledgements

References

Ake, J., Mahrer, K., O'Connell, D., Block, L., 2005. Deep-injection and closely monitored induced seismicity at Paradox Valley, Colorado. Bull. Seismol. Soc. Am. 95 (2), 664–683.

Aki, K., Richards, P.G., 2002. Quantitative seismology.

Atkinson, B.K., 1984. Subcritical crack growth in geological materials. J. Geophys. Res., Solid Earth 89 (B6), 4077–4114.

Bassett, D., Sutherland, R., Henrys, S., Stern, T., Scherwath, M., Benson, A., Henderson, M., 2010. Three-dimensional velocity structure of the northern Hikurangi margin, Raukumara, New Zealand: Implications for the growth of continental crust by subduction erosion and tectonic underplating. Geochem. Geophys. Geosyst. 11 (10).

Beavan, J., Tregoning, P., Bevis, M., Kato, T., Meertens, C., 2002. Motion and rigidity of the Pacific Plate and implications for plate boundary deformation. J. Geophys. Res., Solid Earth 107 (B10).

Bell, R., Holden, C., Power, W., Wang, X., Downes, G., 2014. Hikurangi margin tsunami earthquake generated by slow seismic rupture over a subducted seamount. Earth Planet. Sci. Lett. 397, 1–9.

Bosl, W.J., Nur, A., 2002. Aftershocks and pore fluid diffusion following the 1992 Landers earthquake. J. Geophys. Res., Solid Earth 107 (B12).

Brodsky, E.E., 2006. Long-range triggered earthquakes that continue after the wave train passes. Geophys. Res. Lett. 33 (15).

Brodsky, E.E., Roeloffs, E., Woodcock, D., Gall, I., Manga, M., 2003. A mechanism for sustained groundwater pressure changes induced by distant earthquakes. J. Geophys. Res., Solid Earth 108 (B8).

Chamberlain, C., Hopp, C., 2016. EQcorrscan: EQcorrscan v 0.1.3. Zenodo. http://doi.org/10.5281/zenodo.59976.

Delahaye, E.J., Townend, J., Reyners, M.E., Rogers, G., 2009. Microseismicity but no tremor accompanying slow slip in the Hikurangi subduction zone, New Zealand. Earth Planet. Sci. Lett. 277 (1), 21–28.

Doser, D.I., Webb, T.H., 2003. Source parameters of large historical (1917–1961) earthquakes, North Island, New Zealand. Geophys. J. Int. 152 (3), 795–832.

Elkhoury, J.E., Niemeijer, A., Brodsky, E.E., Marone, C., 2011. Laboratory observations of permeability enhancement by fluid pressure oscillation of in situ fractured rock. J. Geophys. Res., Solid Earth 116 (B2).

Frank, W.B., Poli, P., Perfettini, H., 2017. Mapping the rheology of the Central Chile subduction zone with aftershocks. Geophys. Res. Lett. 44, 5374–5382. https://doi.org/10.1002/2016GL072288.

Geller, R.J., 1976. Scaling relations for earthquake source parameters and magnitudes. Bull. Seismol. Soc. Am. 66 (5), 1501–1523.

Gibbons, S.J., Ringdal, F., 2006. The detection of low magnitude seismic events using array-based waveform correlation. Geophys. J. Int. 165 (1), 149–166.

Goebel, T.H.W., Weingarten, M., Chen, X., Haffener, J., Brodsky, E.E., 2017. The 2016 Mw5. 1 Fairview, Oklahoma earthquakes: evidence for long-range poroelastic triggering at >40 km from fluid disposal wells. Earth Planet. Sci. Lett. 472, 50–61.

Gomberg, J., Reasenberg, P.A., Bodin, P., Harris, R.A., 2001. Earthquake triggering by seismic waves following the Landers and Hector Mine earthquakes. Nature 411 (6836), 462–466.

Hamling, I.J., Hreinsdóttir, S., Clark, K., Elliott, J., Liang, C., Fielding, E., D'Anastasio, E., 2017. Complex multifault rupture during the 2016 Mw 7.8 Kaikōura earthquake, New Zealand. Science 356 (6334), eaam7194.

Hill, D.P., 2008. Dynamic stresses, Coulomb failure, and remote triggering. Bull. Seismol. Soc. Am. 98 (1), 66–92.

Holden, C., Kaneko, Y., D'Anastasio, E., Benites, R., Fry, B., Hamling, I.J., 2017. The 2016 Kaikōura earthquake revealed by kinematic source inversion and seismic wavefield simulations: slow rupture propagation on a geometrically complex crustal fault network. Geophys. Res. Lett. https://doi.org/10.1002/2017GL075301.

Kaiser, A., Balfour, N., Fry, B., Holden, C., Litchfield, N., Gerstenberger, M., Bannister, S., 2017. The 2016 Kaikōura, New Zealand, Earthquake: preliminary seismological report. Seismol. Res. Lett. 88 (3), 727–739.

Kaneko, Y., Nielsen, S.B., Carpenter, B.M., 2016. The onset of laboratory earthquakes explained by nucleating rupture on a rate-and-state fault. J. Geophys. Res., Solid Earth 121. https://doi.org/10.1002/2016JB013143.

Kato, A., Nakagawa, S., 2014. Multiple slow-slip events during a foreshock sequence of the 2014 Iquique, Chile Mw 8.1 earthquake. Geophys. Res. Lett. 41 (15), 5420–5427.

Kato, A., Obara, K., Igarashi, T., Tsuruoka, H., Nakagawa, S., Hirata, N., 2012. Propagation of slow slip leading up to the 2011 Mw 9.0 Tohoku-Oki earthquake. Science 335 (6069), 705–708.

Kilb, D., Gomberg, J., Bodin, P., 2000. Triggering of earthquake aftershocks by dynamic stresses. Nature 408 (6812), 570–574.

King, G.C., Stein, R.S., Lin, J., 1994. Static stress changes and the triggering of earthquakes. Bull. Seismol. Soc. Am. 84 (3), 935–953.

Koulali, A., McClusky, S., Wallace, L., Allgeyer, S., Tregoning, P., D'Anastasio, E., Benavente, R., 2017. Slow slip events and the 2016 Te Araroa M_W 7.1 earthquake interaction: Northern Hikurangi subduction, New Zealand. Geophys. Res. Lett. 44. https://doi.org/10.1002/2017GL074776.

Lohman, R.B., McGuire, J.J., 2007. Earthquake swarms driven by aseismic creep in the Salton Trough, California. J. Geophys. Res., Solid Earth 112 (B4).

Matthews, M.V., Reasenberg, P.A., 1988. Statistical methods for investigating quiescence and other temporal seismicity patterns. Pure Appl. Geophys. 126 (2), 357–372.

McLaskey, G.C., Kilgore, B.D., 2013. Foreshocks during the nucleation of stick-slip instability. J. Geophys. Res., Solid Earth 118 (6), 2982–2997.

Ogata, Y., Katsura, K., 2006. Immediate and updated forecasting of aftershock hazard. Geophys. Res. Lett. 33 (10).

Parsons, T., 2005. A hypothesis for delayed dynamic earthquake triggering. Geophys. Res. Lett. 32 (4).

Peng, Z., Zhao, P., 2009. Migration of early aftershocks following the 2004 Parkfield earthquake. Nat. Geosci. 2 (12), 877–881.

Peng, Z., Vidale, J.E., Houston, H., 2006. Anomalous early aftershock decay rate of the 2004 Mw6.0 Parkfield, California, earthquake. Geophys. Res. Lett. 33 (17).

Peng, Z., Hill, D.P., Shelly, D.R., Aiken, C., 2010. Remotely triggered microearthquakes and tremor in central California following the 2010 Mw 8.8 Chile earthquake. Geophys. Res. Lett. 37 (24).

Perfettini, H., Avouac, J.P., 2004. Postseismic relaxation driven by brittle creep: a possible mechanism to reconcile geodetic measurements and the decay rate of aftershocks, application to the Chi-Chi earthquake, Taiwan. J. Geophys. Res., Solid Earth 109 (B2).

Pollitz, F.F., Stein, R.S., Sevilgen, V., Bürgmann, R., 2012. The 11 April 2012 east Indian Ocean earthquake triggered large aftershocks worldwide. Nature 490 (7419), 250–253.

Prejean, S.G., Hill, D.P., Brodsky, E.E., Hough, S.E., Johnston, M.J.S., Malone, S.D., Richards-Dinger, K.B., 2004. Remotely triggered seismicity on the United States west coast following the Mw 7.9 Denali fault earthquake. Bull. Seismol. Soc. Am. 94 (6B), S348–S359.

Ranero, C.R., Morgan, J.P., McIntosh, K., Reichert, C., 2003. Bending-related faulting and mantle serpentinization at the Middle America trench. Nature 425 (6956), 367.

Reyners, M., Eberhart-Phillips, D., Stuart, G., 1999. A three-dimensional image of shallow subduction: crustal structure of the Raukumara Peninsula, New Zealand. Geophys. J. Int. 137 (3), 873–890.

Ristau, J., 2008. Implementation of routine regional moment tensor analysis in New Zealand. Seismol. Res. Lett. 79 (3), 400–415.

Ristau, J., 2009. Comparison of magnitude estimates for New Zealand earthquakes: moment magnitude, local magnitude, and teleseismic body-wave magnitude. Bull. Seismol. Soc. Am. 99 (3), 1841–1852.

Shelly, D.R., Peng, Z., Hill, D.P., Aiken, C., 2011. Triggered creep as a possible mechanism for delayed dynamic triggering of tremor and earthquakes. Nat. Geosci. 4 (6), 384–388.

Shelly, D.R., Ellsworth, W.L., Hill, D.P., 2016. Fluid-faulting evolution in high definition: connecting fault structure and frequency-magnitude variations during the 2014 Long Valley Caldera, California, earthquake swarm. J. Geophys. Res., Solid Earth 121 (3), 1776–1795.

Toda, S., Stein, R.S., Sevilgen, V., Lin, J., 2011. Coulomb 3. 3 Graphic-Rich Deformation and Stress-Change Software for Earthquake, Tectonic, and Volcano Research and Teaching—User Guide. (No. 2011-1060) US Geological Survey.

Todd, E.K., Schwartz, S.Y., 2016. Tectonic tremor along the northern Hikurangi Margin, New Zealand, between 2010 and 2015. J. Geophys. Res., Solid Earth.

Utsu, T., Ogata, Y., Ritsuko, S., 1995. The centenary of the Omori formula for a decay law of aftershock activity. J. Phys. Earth 43 (1), 1–33.

Vidale, J.E., Shearer, P.M., 2006. A survey of 71 earthquake bursts across southern California: exploring the role of pore fluid pressure fluctuations and aseismic slip as drivers. J. Geophys. Res., Solid Earth 111 (B5).

Waldhauser, F., 2001. HypoDD-A program to compute double-difference hypocenter locations. (No. 2001-113).

Wallace, L.M., Beavan, J., 2010. Diverse slow slip behavior at the Hikurangi subduction margin, New Zealand. J. Geophys. Res., Solid Earth 115 (B12).

Wallace, L.M., Kaneko, Y., Hreinsdottir, S., Hamling, I., Peng, Z., Bartlow, N., D'Anastasio, E., Fry, B., 2017. Large-scale dynamic triggering of shallow slow slip enhanced by overlying sedimentary wedge. Nat. Geosci.. https://doi.org/10.1038/ngeo3021.

Walter, J.I., Meng, X., Peng, Z., Schwartz, S.Y., Newman, A.V., Protti, M., 2015. Far-field triggering of foreshocks near the nucleation zone of the 5 September 2012 (M_W7.6) Nicoya Peninsula, Costa Rica earthquake. Earth Planet. Sci. Lett. 431, 75–86.

Warren-Smith, E., Chamberlain, C., Lamb, S., Townend, J., 2017. High-precision analysis of an aftershock sequence using matched-filter detection: the May 4 2015 ML6 Wanaka earthquake, Southern Alps, New Zealand. Seismol. Res. Lett..

Wells, D.L., Coppersmith, K.J., 1994. New empirical relationships among magnitude, rupture length, rupture width, rupture area, and surface displacement. Bull. Seismol. Soc. Am. 84 (4), 974–1002.

Williams, C.A., Eberhart-Phillips, D., Bannister, S., Barker, D.H., Henrys, S., Reyners, M., Sutherland, R., 2013. Revised interface geometry for the Hikurangi subduction zone, New Zealand. Seismol. Res. Lett. 84 (6), 1066–1073.

Yao, D., Peng, Z., Meng, X., 2015. Remotely triggered earthquakes in South-Central Tibet following the 2004 Mw 9.1 Sumatra and 2005 Mw 8.6 Nias earthquakes. Geophys. J. Int. 201 (2), 543–551.